TITLE: Imaging photoinduced surface potentials on hybrid perovskites by real-time Scanning Electron Microscopy.

Authors:

Gabriele Irde[a,b]   gabriele.irde@polimi.it

Silvia Maria Pietralunga *[b,c],   silvia.pietralunga@ifn.cnr.it   * corresponding author

Vittorio Sala [a,b],   vittorio.sala@polimi.it

Maurizio Zani [a],   maurizio.zani@polimi.it

James M. Ball [b1],   james.ball@physics.ox.ac.uk

Alex J Barker [b],   Alex.Barker@iit.it

Annamaria Petrozza [b],   Annamaria.Petrozza@iit.it

Guglielmo Lanzani[a,b]   Guglielmo.Lanzani@iit.it

and Alberto Tagliaferri[a,b]   alberto.tagliaferri@polimi.it

[a] *Dipartimento di Fisica, Politecnico di Milano, Piazza Leonardo da Vinci 32, Milano, Italy*

[b] *CNST@PoliMi, Istituto Italiano di Tecnologia (IIT), Via Giovanni Pascoli 70/3, Milano, Italy*

[c]*Istituto di Fotonica e Nanotecnologie (IFN), CNR, Piazza Leonardo da Vinci 32, Milano, Italy*

Declarations of interest: none

---

[1] James M. Ball's present address: Department of Physics, University of Oxford, Department of Physics Parks Road OX1 3PU, UK

ABSTRACT

We introduce laser-assisted Time-Resolved SEM (TR-SEM), joining Scanning Electron Microscopy and laser light excitation, to probe the long-term temporal evolution of optically excited charge distributions at the surface of Metal Ammonium Lead Triiodide (MAPbI$_3$) hybrid perovskite thin films. Laser-assisted TR-SEM relies on the optically induced local modification of Secondary Electron (SE) detection yield to provide mapping of photoexcited potentials and charge dynamics at surfaces, and qualifies as a complementary approach to near-field probe microscopies and nonlinear photoemission spectroscopies for photovoltage measurements. Real-time imaging of evolving field patterns are provided on timescales compatible with SEM scanning rates, so that temporal resolution in the millisecond range can be ultimately envisaged. ~~while shorter timescales down to the ultrafast regime can be accessed by a pump-probe approach~~. MAPbI$_3$ is an outstanding light-sensitive material candidate for applications in solar light harvesting and photovoltaics, also appealing as an active system for light generation. In this work, the real time temporal evolution of optically induced SE contrast patterns in MAPbI$_3$ is experimentally recorded, both under illumination by a 405 nm blue laser and after light removal, showing the occurrence of modifications related to photoinduced positive charge fields at surface. The long term evolution of these surface fields are tentatively attributed to ion migration within the film, under the action of the illumination gradient and the hole collecting substrate. This optical excitation is fully reversible in MAPbI$_3$ over timescales of hours and a complete recovery of the system occurs within days.

Permanent irradiation damage of the material is avoided by operating the SEM at 5keV of energy and 1-10pA of primary current. Optical excitation is provided by intense above-bandgap illumination (up to 50W/cm^2). TR-SEM patterns show a strong dependence on the geometry of SE collection. Measurements are taken at different axial orientations of the sample with respect to the entrance of the in-column detection system of the SEM and compared with numerical modeling of the SE detection process. This enables to single out the information regarding the local potential distribution. Results are interpreted by combining data about the spectral distribution of emitted SEs with the configuration of the electric and magnetic fields in the specimen chamber. The present modeling sets a robust basis for the understanding of photoinduced SE electron contrast.

KEY WORDS

Real-time Scanning Electron Microscopy; Time-Resolved Scanning Electron Microscopy; Organic-inorganic perovskite; Photovoltage; Secondary electron emission.

1. INTRODUCTION

Scanning Electron Microscopy (SEM) is a consolidated technique, widely used in morphological characterization at the nanoscale. SEM imaging by Secondary Electron (SE) detection is intrinsically sensitive to the presence of local space charge fields and voltage distributions at surfaces. Actually, charging and related parasitic effects may interfere with the emission and collection of the SEs up to the point where artifacts seriously jeopardize the reliability of the results (Cazaux, 2004; Seiler, 1983). However, this same sensitiveness to local charges and potentials has been turned into an opportunity and profitably exploited to widen the scope of application of imaging by SEM beyond the mere morphological visualization. For instance, the modulations in SE contrast issued by surface polarization and space fields can be exploited to image heterostructures as well as differently doped regions in semiconductors (El-Gomati and Wells, 2001; Elliott et al., 2002; Kazemian et al., 2006; Sealy et al., 2000; Tsurumi and Hamada, 2013; Xu et al., 2013). In these cases, SE contrast originates from variations in the value of work function, from electrical charge redistribution and from local electric fields which affect the trajectories of emitted SEs and the collection yield (Cazaux, 2012, 2010; Chee et al., 2011; El-Gomati et al., 2005; Volotsenko et al., 2010). The impact of local surface fields on the SE trajectories and ultimately on measured SE contrast can be estimated by numerical modeling of the processes of SE emission and detection. In principle, SEM sensitivity to local surface fields applies whatever is the source of charge unbalance. Specifically, optical excitation of charge carrier population at surface may lead to local modulation of the work function and to photovoltages and be imaged by SEM as SE contrast pattern. Extended review papers on photovoltage phenomena and related characterizations "at the crossroads of physics, chemistry and electrical engineering" have been provided e.g by Kronik and Shapira (Kronik and Shapira, 2001, 1999). Among commonly used experimental methods to evaluate the effect we can mention photo-assisted Kelvin probe spectroscopy (Ali Deeb et al., 2017), all-optical pump-probe absorption spectroscopies (Jana et al., 2014) and photoemission electron spectroscopies (Tanaka, 2012).

 The advantage of SEM, if compared to other measurement techniques, is the combination of surface selectivity and 2D mapping over a wide range of view fields with its lateral resolutions at the nanoscale. Such features are specifically useful when studying optical beam sensitive photoelectrical and photovoltaic materials, where a major role in defining the figures of merit for energy conversion is played by photo-physics and photo-chemistry at surfaces and interfaces (Chiarello et al., 2017; Lanzani, 2012; Wuerfel, 2009). The idea of detecting electrons emitted from the illuminated surface of a semiconductor as a non-contact means to probe local photovoltage values actually traces back to the 1990s. In a first patent by Flesner, the energy spectra of SEs emitted from illuminated and dark regions in a semiconductor are compared, while probing different sites on the sample surface by scanning the Primary Electron (PE) beam (Flesner, 1990). Alternatively, photoelectrons are emitted as a consequence of illuminating the sample by UV light (around 6eV) and spectrally analyzed and detected, to probe the electrical potential at the material surface (Flesner, 1992). Regarding the temporal evolution, the dynamics of photoexcited electrical phenomena at surfaces may vary over an extreme range of timescales, from quasi-CW (continuous wave) to ultrafast regimes. Light-assisted SEM analyses can be provided with Time-Resolved detection schemes (TR-SEM), conceived and designed to address the different dynamical ranges. Ultrafast dynamics in photoinduced

SE contrast have actually been retrieved stroboscopically, by exploiting pulsed PE beams (May et al., 1987) and in pump-probe configurations (Cho et al., 2014; Liao and Najafi, 2017; Mohammed et al., 2011). Specifically, ultrafast SEM monitors light-induced charge dynamics, deriving out-of-equilibrium and hot-charge transport parameters at semiconductor surfaces and *pn*-junctions. Its application to study charge dynamics in insulating systems has also been recently demonstrated by some of the authors (Zani et al., 2018).

Commercial SEM are capable of real-time imaging (compatible with raster scanning frequency) down to the milliseconds, so that optically excited charge transport phenomena evolving on these temporal scales may in principle be studied in a dynamical real-time TR-SEM. Materials and devices for photoelectric energy conversion are a case study for TR-SEM operating in real-time, as dynamical mapping of the distribution of surface photoexcited charge fields and voltages may provide insight into the factors influencing their performances.

In this work we present a light-assisted TR-SEM apparatus, to image *in-situ* excited photo-physical phenomena by performing real-time SE detection on the timescale of few tens of seconds and up to several hours. To this aim, pump laser light is coupled into the SEM measurement chamber to illuminate the sample, to provide dynamical maps of optically induced voltages at surfaces. A numerical model of the process of SE detection has also been developed to provide an insightful interpretation of the experimental results.

We have exploited real-time TR-SEM to visualize light-induced modifications in hybrid perovskite Methylammonium Lead Trihalide-*MAPbI$_3$* (CH$_3$ NH$_3$PbI$_3$), considered among the most promising candidates to fabricate high performance solar cells (Snaith, 2013; Wu et al., 2017). Sub-micron hybrid perovskites thin films feature extremely high power conversion efficiencies (PCE) -above 23% ("NREL's "Best Research-Cell Efficiencies" Chart," 2018) reached in laboratory environment. However, the heterogeneity at the local level, as well as instability and degradation issues over long temporal scales ascribable to photo-chemical and photo-electronic mechanisms (Deng et al., 2015a; Gottesman et al., 2015; Leijtens et al., 2015; Xing et al., 2016; Yuan et al., 2016), still prevent reliable in-field exploitation of this nanostructured system. A full comprehension of the physics and chemistry at the origin of these issues has not been reached so far and TR-SEM analyses contributes with novel data.

The following Section describes the experimental setup of TR-SEM and introduces the analyses on *MAPbI$_3$*. The regime of operation has been optimized to avoid both electron and optical beam damaging of the material. In the Section dedicated to Results, TR-SEM operation is illustrated by means of selected key-examples. If contamination by moisture is avoided, as it may occur under vacuum conditions in SEM environment, no permanent damage in the material is registered even under intense and above-bandgap optical excitation (up to ~50 W/cm^2). Therefore, in the present case of free MAPbI$_3$thin films, the evolution of optically-excited space charge domains is fully reversible over timescales of hours. The interpretative model has been developed at the aid of a numerical simulation for the SE detection process in the specific experimental environment. In the present case of characterization on perovskite thin films, TR-SEM results are discussed in the light of existing literature and support the occurrence of light-induced structural modifications attributed to ion migration, leading to long term evolution of reversible photoinduced charge fields at MAPbI$_3$ surface, as reported and discussed in the final Section.

2. MATERIALS AND METHODS

2.1: Setup and principle of operation of TR-SEM

The general scheme of light-assisted TR-SEM experimental apparatus is represented in Fig.1a. A commercial High-Resolution Field-effect SEM (*Tescan MIRA III*) is customized by providing optical access to the specimen chamber through optical windows. The SEM is operated in High Vacuum at a pressure range of $5 \cdot 10^{-4} \div 5 \cdot 10^{-5} \, Pa$ and an *in-column* Everhart-Thornley (ET) SE detector is used, with an acceleration grid at +300V and a +10kV scintillator. The ET detector is operated in linear regime, adjusted to avoid any saturation of the contrast. The latter is digitized over 2^{16}=65536 gray levels. Images are recorded in frames of 768 x 1024 pixels. Pixel dwell time ranges between 10 and 32 µs/pixel, corresponding to image recording times of 7.8s and 25s, respectively. The present investigation on the evolution of light-assisted SE contrast is performed with the SEM operated in *field* mode, meaning that the magnetic objective lens is switched off. In this configuration, the detection system substantially operates under conditions of cylindrical symmetry, without affecting the validity of the results in terms of spatial resolution. Operation in *field* mode and related levels of magnification are also compatible with the need to keep optical pump-electron probe conditions.

The optical beam from a diode laser, emitting deep blue light at $\lambda = 405 nm$ (3.061 eV) in continuous-wave operation, is expanded in a 1 x 4 telescope, spatially filtered to improve transversal mode selectivity, steered into the SEM specimen chamber and focused onto the sample within the SEM field of view. The optical bench support is rigidly connected to the SEM. The geometry of excitation and detection is schematically reported in Fig.1b. The reference system, fixed with the specimen chamber, has its *z*-axis coincident with the axis of the SEM column. Samples are mounted on a sample holder with two independent angular degrees of freedom. The sample holder can be azimuthally rotated by angle ϕ in the horizontal plane (around the z axis) and tilted by angle θ ~~around the x axis~~, so as to vary the inclination of the normal direction of the sample surface with respect to the axis of the SEM column. The laser beam is directed onto the sample surface at an incidence angle $\gamma = 70° \div 80°$, to minimize photon scattering <u>towards</u> the detector.
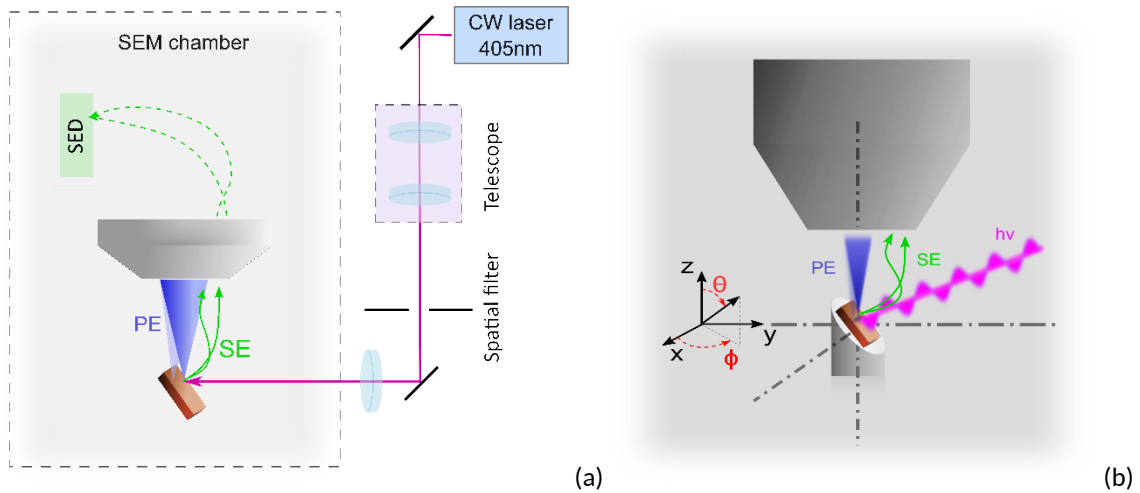
Fig. 1: Schematic representation of TR-SEM setup. (a): the specimen chamber with free-space propagating laser beam focused onto the sample in the view field of the SEM. Incident Primary Electrons (PE) and emitted Secondary Electrons (SE) are indicated. SE are collected at the in-column detector (SED) (b): reference measurement geometry, showing azimuth angle ϕ and tilting angle θ around the x-axis. Angles ϕ e θ define the normal direction to the surface of the sample. The laser beam is also shown, incident on the surface at an angle γ (not indicated). **[NO COLOR PRINT]-[SMALL COLUMN SIZE]**

2.2: TR-SEM on Methyl-Ammonium Lead Triiodide thin films

TR-SEM has been applied to investigate the temporal evolution of photoexcited space charge dynamics at the surface of Methyl-Ammonium Lead Triiodide (MAPbI3) thin films, which are exploited as active absorbing layers in Planar HeteroJunction (PHJ) perovskite solar cells(Snaith, 2013).

~~The structure of Semiconductor hybrid perovskites have general chemical formula ABX3 is shown in Fig.2a, where A represents the methyl-ammonium cation CH3NH3+, B is the metallic cation (Pb2+) and X is the halide ion (I-).~~ MAPbI3 films 350nm-thick have been deposited by the two-step interdiffusion method (Xiao et al., 2014c) onto clean indium-tin oxide (ITO) coated glass substrates and with a poly(3,4-ethylenedioxythiophene) polystyrene sulfonate (PEDOT:PSS) interlayer. The structure of the sample under test is schematically represented in Fig.2b. The multilayered stack is part of the so-called "inverted" solar cell structure, <u>where </u>the MAPbI3 film is ultimately sandwiched between a hole transport layer (HTL, the p-type side of the solar cell junction), the PEDOT:PSS film in this case, and an electron transport layer (ETL, the n-type side of the junction) provided by a PCBM film connected to a metallic film electrode (De Bastiani et al., 2016). <u>Solar cells fabricated in the inverted structure and using perovskite absorbers deposited by the two-step interdiffusion method are demonstrated to reach best PCE values above 15 %, a Fill Factor around 80% and negligible hysteresis (Xiao et al., 2014a, 2014c).</u>
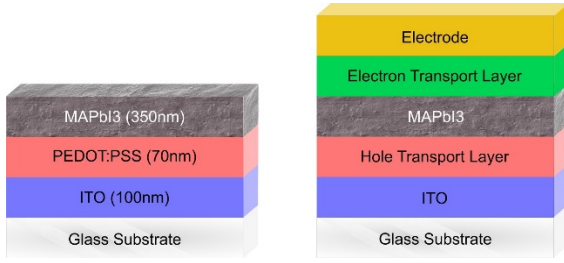
Fig. 2: the structure of the sample under test with the neat MAPbI$_3$ film exposing its free surface, and a reference stack structure of the inverted Planar Hetero Junction solar cell.
[NO COLOR PRINT]-[SMALL COLUMN SIZE]

Deposited neat MAPbI$_3$ films are polycrystalline, as shown in the SEM image in Fig.3a, with a distinctive heterogeneous surface (Wu et al., 2017).
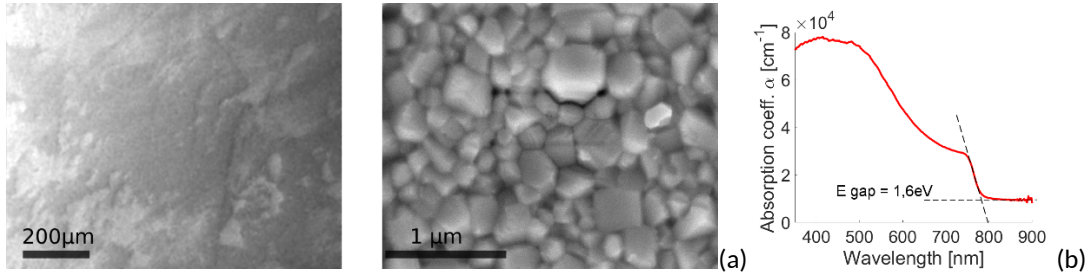

Fig.3. (a): SEM images of the surface of neat MAPbI$_3$ films, 350nm thick, deposited on PEDOT:PSS, showing the polycrystalline structure and typical surface heterogeneity; (b): absorption coefficient in the VIS and near IR optical range. Blue light is completely absorbed within the thickness of the film.
[NO COLOR PRINT]-[SMALL COLUMN SIZE]

Optical transmittance measurements are reported in Fig.3b. Estimated threshold absorption wavelength $\lambda = 775nm$ corresponds to an optical energy gap at $E_g = 1.6\ eV$, in substantial agreement with reported data in the literature (Hoke et al., 2015; Yamada et al., 2014). Above-bandgap blue light at $\lambda = 405nm$ *(3.0 eV)* is therefore strongly absorbed. Actually, an absorption coefficient $\alpha \sim 7x10^4\ cm^{-1}$ can be estimated over the blue range, corresponding to an absorption length $\alpha^{-1} \sim 140nm$ and implying that the 350nm-thick film absorbs more than 90% of the incident light. In TR-SEM configuration, the exciting laser beam is focused on the sample surface over an elliptical area measuring about 20000 μm^2 (minor axis $\sim 100\mu m$). Incident optical power measures $\sim 10\ mW$, corresponding to a maximum beam intensity $I \sim 50W\ cm^{-2}$ and to a CW photon flux $\sim 10^{20} ph/cm^2$. Above-bandgap optical absorption promotes free electrons and holes pairs in the MAPbI$_3$ semiconductor. The local density of photoexcited free charges within one absorption length from the surface has been estimated by solving generation and recombination rate equations in steady state under the hypothesis of single-photon (linear) absorption (Srimath Kandada et al., 2016). Quasi-neutrality regime and free carriers lifetimes in the order of 100ns are assumed, as limited by trap-assisted and bimolecular recombination (Xiao et al., 2014a; Yamada et al., 2014). Estimated

value for free charge density at 10nm below the surface is $\sim 10^{17} cm^{-3}$ and exponentially decreasing in depth according to Lambert-Beer law.

The values of optical intensity for the exciting laser beam have also been chosen so as to keep a safety factor of 10 with respect to ascertained threshold for permanent optical damage in metal halide perovskite thin films (Yuan et al., 2016). Actually, photo-chemical reactions can induce material dissociation and permanent morphological modifications. At our experimental conditions, optically induced permanent morphological damage is excluded by highly magnified ($M = 50K\ x$) SEM images, taken 10 minutes after illuminating for 480 seconds at maximum intensity and showing no sign of morphological modification at the microscale. The absence of permanent damage is also favored by high vacuum conditions, strongly decreasing the effects of oxygen and moisture, which are major causes of oxidation of MAPbI$_3$ and contribute to the degradation of the material under illumination (Leijtens et al., 2015). A differential image taken from Figure 4a and 4b is reported as Supplementary Information (Figure S.I.1) which highlights a slight photo-induced contrast modulation located at grain boundaries and lasting over several minutes. This grain boundary modulation might be contributed by light-induced long-lasting local space-charge domains, in agreement with what recently investigated e.g. by Gomez and co-workers by Photoconductive AFM and PL microscopy (Gomez et al., 2018)
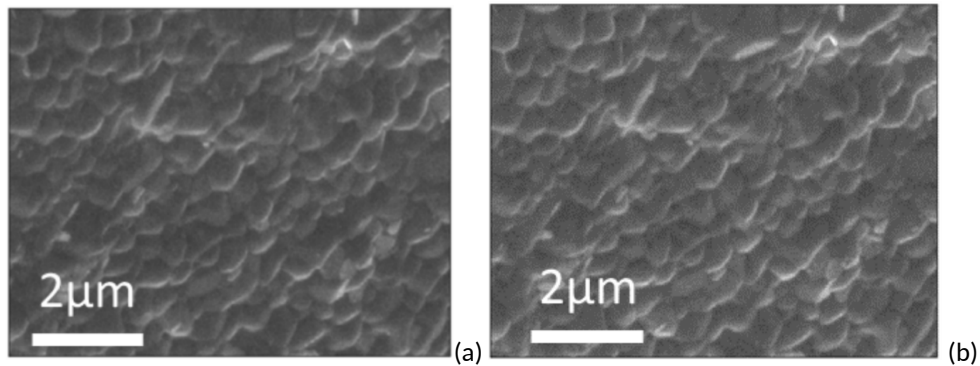

Fig.4: SEM high magnification images M=50k of the pristine area of MAPbI$_3$ sample (a) and after being irradiated at $I \sim 50\ W$ cm^{-2} for 480 seconds (b), showing no evidence of optically induced morphological damaging.
[NO COLOR PRINT]-[SMALL COLUMN SIZE]

MAPbI$_3$'s partially organic composition also makes it particularly sensitive to electron beam damaging under SEM investigations. Yuan and coworkers (Yuan et al., 2016) reported about the occurrence of permanent e-beam damage of combined chemical and structural origin induced in MAPbI$_3$ films. At a PE current of 86pA@10kV, corresponding to an estimated dose of about $10^{15} el/cm^2$ at experimental conditions there reported, ion migration and chemical decomposition occurs, which under vacuum condition may even cause the removal of high vapor pressure materials, leading to strong and permanent modifications of the composition of the film and even morphological alterations.

To minimize the risk of e-beam damaging of the sample (Cazaux, 2004), TR-SEM characterization is performed at 5kV of PE acceleration voltage, which is reported not to affect photo-physical properties of metal-halide perovskites (Yuan et al., 2016). Under SEM testing conditions as used in the present context, e-beam damaging is most likely originated by hydrocarbon contamination (Egerton et al., 2004), even if in case of hybrid perovskite systems also a certain contribution from radiolysis and chemical decomposition at the molecular level could not be excluded *a-priori*. The effects of surface contamination by hydrocarbons on the SE emission spectral curve and on SEM contrast patterns (Cazaux, 2010) may be complex, and a full treatise on their mechanisms in perovskites films will not be given here. For the purposes of the present work the threshold for e-beam damaging has been experimentally estimated as the critical electron dose which permanently modifies the SE contrast on an irradiated zone. This has been evaluated by , as is evidenced by taking images of the MAPbI$_3$ surface at different increasing magnifications, as reported in details as Supplementary Information and in Figure SI.2. A threshold dose of $2 \cdot 10^{14} el/cm^2$ is found, equivalent to irradiating an area of $180x180\mu m^2$ with a PE current of 100pA for 16s. Therefore, to keep sub-threshold damaging conditions during TR-SEM, a PE current of $5 \div 10\ pA$, a pixel size of $1\mu m^2$ and a pixel dwell-time between 10 μs and $32\mu s$ have been used throughout all experiments, leading to recording times of respectively 7s and 25s per image and to a maximum electron dose $\sim 2 \cdot 10^{11} el \cdot cm^{-2}$ for the longest dwell-time. The need to keep the perturbation induced by the electron probe negligible with respect to the effects optically induced by the laser pump, combined with the fact that the electron dose increases with the second power of image magnification M, may limit the feasibility of high-resolution TR-SEM imaging in strongly e-beam sensitive materials. It may also represent an issue in cases when optical damaging poses a strict upper limit to the level of optical fluence. In the present case, a magnification $M = 250x \div 400x$ is chosen, also keeping the illuminated area fully within the viewfield.

Monte Carlo calculations of the trajectories of PEs at 5keV in the perovskite stack have been assessed using CASINO 2.4.8.1 simulation environment (Drouin et al., 2007). Results are reported in Fig. 5, showing that PE penetration depth is limited to the thickness of the MAPbI$_3$ film, without affecting the underlying layers. Therefore, photoinduced surface field is the expression of a polarization which entirely develops within the MAPbI$_3$ volume.
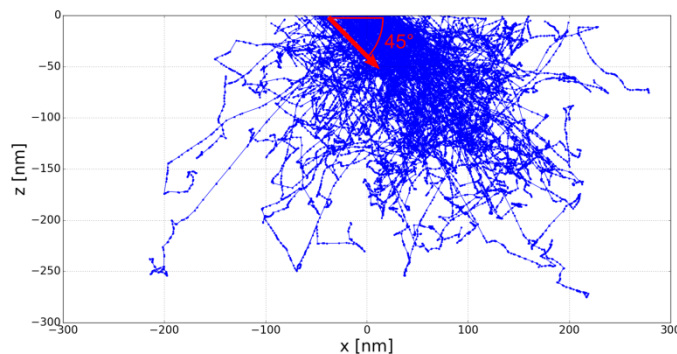

Fig. 5: MonteCarlo simulation of the trajectories of PEs at 5keV of primary kinetic energy, in the thickness of the MAPbI$_3$ film, without affecting the layers underneath.
[NO COLOR PRINT]-[SMALL COLUMN SIZE]

Besides avoiding permanent damaging, the choice of optical and electronic parameters also assures that the energy deposited over the excited volume by incident pump photons – at a photon dose estimated in the $\sim 10^{20} \div 10^{22} cm^{-2}$ range- overcomes by three orders of magnitude the contribution of the e-beam probe, stating that the optical induced perturbation greatly exceeds e-beam induced one.

3.   RESULTS

3.1   Differential TR-SEM contrast images

In SEM analyses, SE contrast patterns (Chee et al., 2008; Seiler, 1983) are generally contributed by sample morphology and by local differences in the values of the work function. In TR-SEM the SE contrast is also contributed by the variations that illumination induces in the material and which affect the processes of emission and collection of SEs. One of the most valuable information concerns electrical space charge fields that build-up at semiconductor surfaces as a consequence of optical absorption. Space charge in turn modifies the local value of the work function and SE emission. Locally modulated work function also issues polarization *patch fields* in the vacuum volume adjacent to the surface, which affect SE trajectories and collection at the detector.

The dynamical evolution in light-induced SE contrast is shown by acquiring TR-SEM images after selected time intervals during CW illumination and then by periodically taking images after turning the laser off, to record the decay of SE contrast along several minutes. SEM images are also collected after several hours of permanence in the dark, to check for residual long-lasting laser-induced effects.

In order to retrieve information about light-assisted SE contrast and to disentangle the morphological contribution, a procedure of differential processing of detected SE images has been developed, as exemplified in Fig. 6 and detailed in the following. TR-SEM images have been acquired in *asymmetric* detection geometry at $\phi = 30°$ and tilt $\theta = 45°$. The first row of Fig. 6 (labelled as *a*) shows raw SEM data. The frame on the left (label *ref*) is the reference image of the pristine sample, taken in any series of measurements before illumination to record the morphological contribution to SE contrast. As the light is turned on (column label *on*), the overall brightness increases due to scattered photons detected at ET, while a dark spot appears in correspondence with the position of the laser beam, indicating a reduced SE collection. The dashed ellipse highlights the laser spot on the surface of the MAPbI$_3$ film. The elliptical mark results from stretching the cross section of the free propagating Gaussian beam by the projection factor $1/\cos(\gamma)$. As already stated, by using incidence angles $\gamma = 70° \div 80°$ photon scattering at the detector is minimized. On switching the laser beam off, (column label *off*) the bright background vanishes, but the modulation in SE contrast located at the position of the laser spot is still visible.
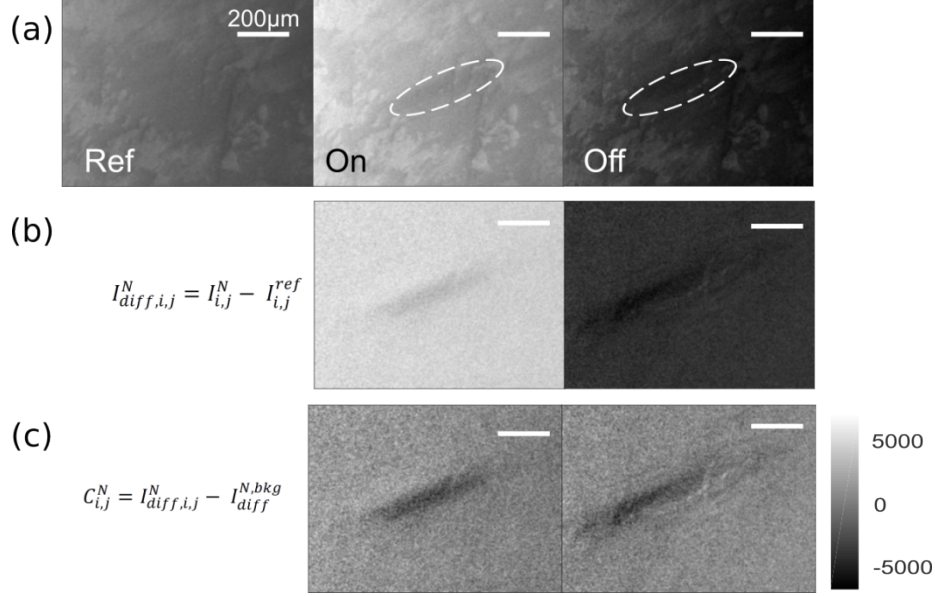
Fig. 6: *TR-SEM images, showing the raw acquired data and the result of image post-processing. The spatial scalebar is common to all images. Dashed ellipses highlights the laser spot on the sample surface. In row (a): (column label: ref) Pristine sample before illumination. This image is taken as reference for further processing; (column label: on) SE contrast immediately after turning on the laser; (column label: off) SE contrast immediately after turning off the laser. In row (b): differential TR-SEM images, where reference image has been subtracted from raw images, in columns labeled (on) and (off) respectively. In row (c): final $C_{i,j}^N$ differential contrast images, after background subtraction, respectively corresponding to the (on) and (off) cases respectively. A grey level offsetting to medium grey is observed.*
[SMALL COLUMN SIZE]

Optically induced effects are barely perceptible in the as-taken SEM images reported in the upper row of Fig. Detected raw SE images are then differentially processed as explained hereafter. A preliminary 2D Gaussian smoothing (with σ equal to three pixels) is performed in each one of the images over the values of grayscale measured at pixels *(i,j)*. Then, differential contrast images are obtained from each one of the N-th contrast images taken under (or after) illumination. This is operated by a pixel-by-pixel subtraction of the value of the gray level measured at pixel *(i,j)* in the N-th image, $I_{i,j}^N$, and the corresponding gray level in the reference image $I_{i,j}^{ref}$, that leads to:

$$I_{diff,i,j}^N = I_{i,j}^N - I_{i,j}^{ref}.$$
(1)

The results are shown in row *(b)* of Fig.6. The contribution to the SE contrast from morphology and work function modulation of the pristine sample is drastically reduced and light-induced contrast is enhanced. The laser footprint appears in the shape of an elliptical region of dark SE contrast.

The final differential SE contrast images are then defined as:

$$C_{i,j}^N = I_{diff,i,j}^N - I_{diff}^{N,bkg},$$
(2)

and obtained by subtracting to $I_{diff,i,j}^N$ a background level $I_{diff}^{N,bkg}$, defined as a spatial average of $I_{diff,i,j}^N$ values measured outside the illuminated spot.

Examples of corresponding differentially processed and renormalized images are shown in row *(c)* of Fig. 6. The subtraction of an averaged background is a linear correction which eliminates the contribution to SE contrast due to other causes than local optical excitation, though not accounting for non-linear effects and interdependences. In this way, also the averaged bright background contribution, which occurs under illumination due to scattered photons, is removed and optically induced contrast maps $C_{i,j}^N$ can be compared. Processed images clearly show a dark contrast area under illumination and the rise of a dipolar contrast configuration as illumination is turned off. Background subtraction is necessary to improve the visibility of the photoinduced SE contrast, which in the strongest case amounts to about 5% of the background value and in general, to decouple the measurement from background fluctuations which may occur between different images within a temporal series. It is worth also noticing that the same parameters of brightness and contrast for the ET detector are used all along each one of the temporal series of images.

3.2: Geometrical dependence of TR-SEM contrast patterns

Since surface orientation and collection geometry crucially affect SE detection yield (Cazaux, 2010; Konvalina and Müllerová, 2006; Müllerová and Konvalina, 2009) TR-SEM contrast patterns have also been recorded at different orientations of the sample with respect to the column axis, as shown in Fig. 7 and Fig.8.

The *field* mode of operation of the SEM combined with *in-column* detection is at the origin of a z-axis cylindrical symmetry in detection which can be observed in the set of images reported in Fig. 7, that shows the effect of tuning the azimuthal angle ϕ. Images are collected after exposing the sample to laser light for 4 minutes and then leaving it in the dark for approximately 20 minutes to let the system evolve onto a quasi-stable condition. Again, dipolar contrast patterns are generated, similarly to what shown in Fig. 6. The angle ϕ is changed to one of twelve discrete values sampling the full roundabout while keeping the sample surface normal at $45°$ from the electron column axis. ~~tilt angle fixed at $\theta = 45°$.~~ No significant variation of the contrast over the illuminated area is evident, apart from the azimuthal rotation.
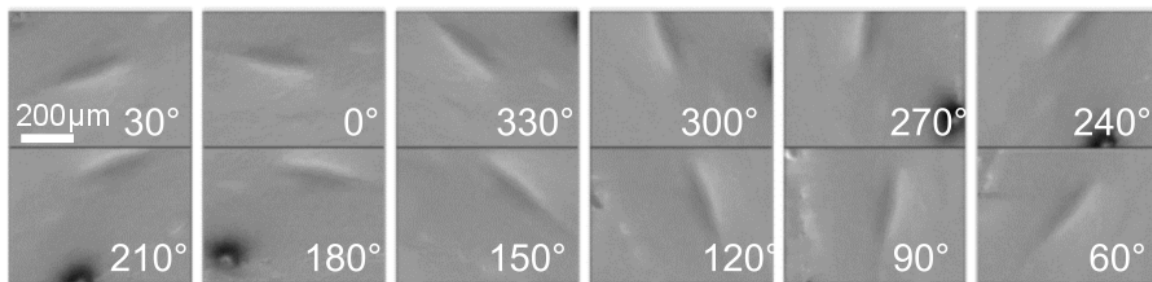

Fig. 7: Effect of horizontal rotation ϕ on TR-SEM contrast on MAPbI$_3$. Measurements are taken in the dark after equivalent illumination conditions. The outcome is a plain roundabout of the frame, with the laser mark following the ϕ rotation.

[1.5 COLUMN SIZE]

Instead, different orientations of the sample with respect to the <u>detection axis (that coincides with the electron column axis in *field mode*)</u> ~~entrance of the detection system~~ strongly affect the appearance of the $C_{i,j}^N$ contrast maps. Fig. 8 shows the effects induced on TR-SEM images by changing <u>the</u> ~~tilt~~ angle θ <u>between the sample surface normal and the electron column axis</u> at fixed azimuthal angle $\phi = 0$, after exposing the sample to the laser beam in the same conditions as in Fig. 7. In Fig. 8a a series of differential images taken at different tilt angles is reported. The corresponding cross-sectional profiles, extracted across the direction marked by the arrow, are shown in Fig. 8b. In passing from negative to positive values of θ, evidently also the contrast pattern inverts its sign. Moreover, in correspondence to $\theta = 0$, i.e. when the sample normal is parallel to the axis of the electron column, TR-SEM contrast <u>within the illuminated area</u> looks plain dark.
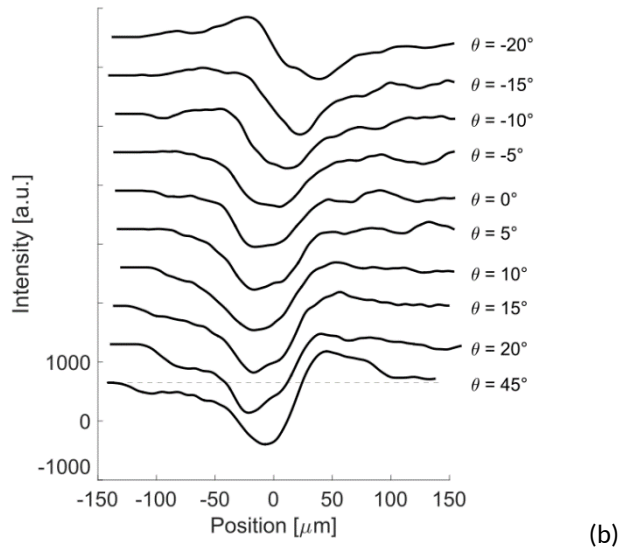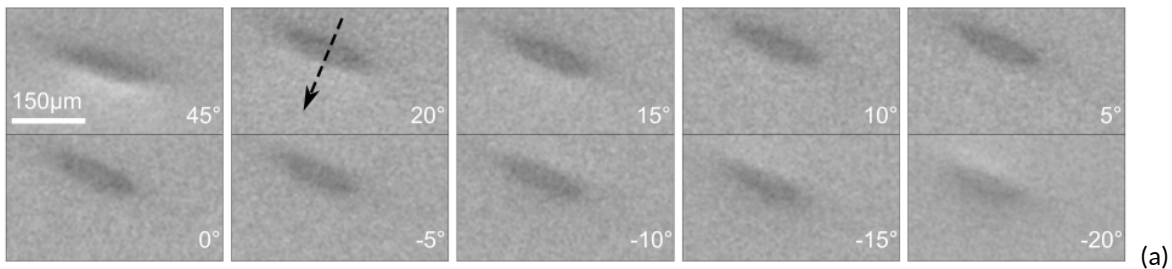

(a)

(b)

Fig. 8: Effect of tilting angle θ on TR-SEM contrast on MAPbI$_3$. Measurements are taken in the dark after equivalent illumination conditions.(a): differential contrast maps measured at different tilting angle; (b): cross-section profiles corresponding to maps in (a). As tilt angle changes sign, also the photoinduced contrast is reversed.
1.5 COLUMN SIZE]

3.3: Temporal evolution of Light-assisted TR-SEM contrast

Temporal series of images of photo-induced TR-SEM contrast in MAPbI$_3$ have been acquired at experimental conditions such as to avoid permanent damaging by electron and photon beam irradiation. Fig. 9 shows an example of long term evolution of photoinduced contrast in dark. Differential $C_{i,j}^N$ patterns in frames (b-d) are acquired respectively 16 min, 24 hours and 72 hours after switching illumination off, respectively. The photoinduced pattern is clearly visible in frame (b) and its contrast amplitude slowly decreases, recovering towards the SEM image of the pristine sample as shown in frames (c) and (d). This is an indication that, in the absence of any permanent damage, optically induced TR-SEM contrast is reversible and characterized by recovery times that can last up to many hours.
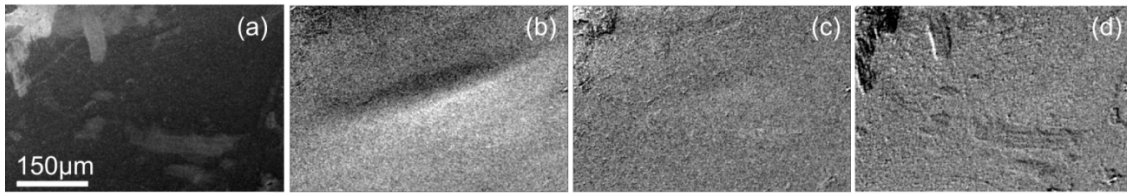

Fig. 9: Long term persistence of the SE contrast perturbation and recovery of pristine conditions at long timescales. Photon dose is 2,5x10^{22} ph/cm^2. (a): raw morphological image of pristine surface; (b) TR-SEM contrast after 16 minutes in dark; (c) after 24 hours in dark; (d) after 72 hours in dark.
[1.5 COLUMN SIZE]

A deeper insight in the TR-SEM contrast dynamics in MAPbI$_3$ can be obtained from the temporal series in Fig. 10, acquired in the same geometry as in Fig. 6 ($\phi = 30°$ and $\theta = 45°$). The sample is illuminated for 480s and then kept in the dark for further 480s. TR-SEM patterns in Fig. 10a are acquired along the first 180s under illumination and then along the first 180s in the dark.

Under illumination, the main feature in $C_{i,j}^N$ images is a dark area at the laser spot, corresponding to a negative contrast. As the exposition progresses along the first 180s, the dark area widens and the amplitude of the contrast increases. A faint dipolar contrast is also visible, at the edges of the dark region. As the laser is switched off, a more complex contrast pattern appears within the acquisition time for one single frame, with sharper bright and dark sides, opposite to the case under illumination and also evolving on the timescale of a few minutes. Related $C_{i,j}^N$ contrast profiles are extracted by cross-sectioning the illuminated elliptical areas along the minor axis and are shown in Fig. 10b. At laser on, contrast profiles are dark and bell-shaped in correspondence with the laser beam spot. A zone of brighter differential contrast arises, aside of the illuminated area and in the region of the sample closer to the entrance of the detection system. As the laser is turned off, the profiles change their shape over a switching time in the range of a few seconds, and the sharp dipolar SE contrast clearly appears, while the region of sample closer to the column turns darker than the background and the region away from the column turns brighter.
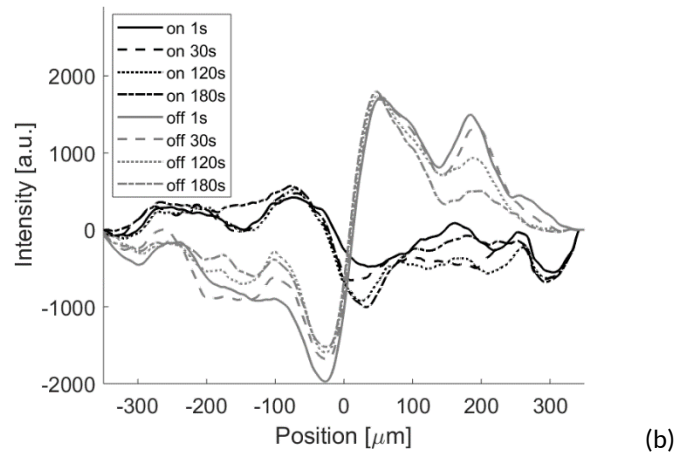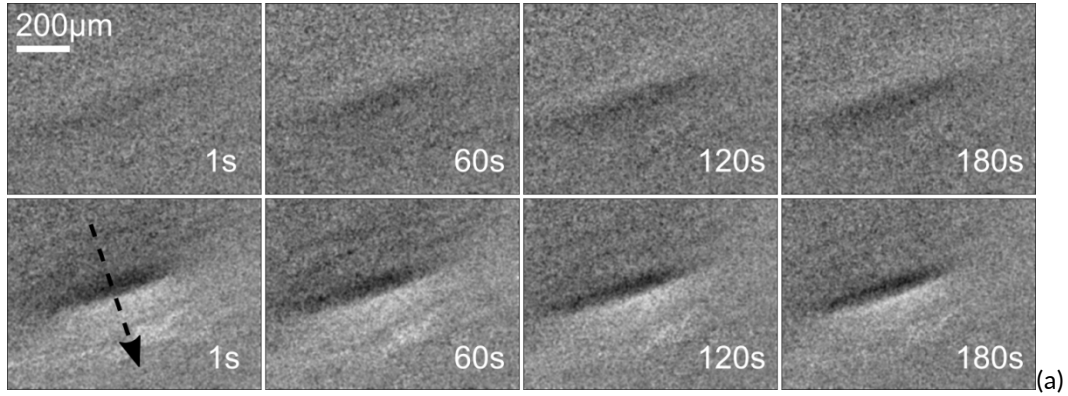
14

Fig. 10: evolution in the TR-SEM contrast in time, shown by the sequence of differential images, detected at $\phi = 30°$ and $\theta = 45°$. (a): Differential patterns recorded under illumination at several times along 180s and subsequently during 180s in the dark; (b): related contrast profiles, measured along the minor axis of the elliptical illuminated zone, as marked in (a).

[[1.5 COLUMN SIZE]

3.4: Numerical modelling of TR-SEM detection

The optically induced dipolar TR-SEM contrast patterns and their evolutions can be discussed in the frame of local photovoltaic effects at the surface of MAPbI$_3$ films. In the formation of SEM images, a key role is played by the process of SE collection at the detector under the effects of electric and magnetic fields in the specimen chamber (Müllerová and Konvalina, 2009). Localized potential distributions at surfaces and corresponding *patch fields* affect the trajectories of emitted SEs, in dependence on their kinetic energy and emission point. All these effects must be taken into consideration for a correct interpretation of the experimental results when using SEM to map local charge distributions (Cazaux, 2008, 2004).

A proof of concept scheme is provided by simulating the operation of light-assisted TR-SEM in *Simion 8.0* numerical environment (Manura and Dahl, 2008). The collection efficiency at SEM detector is evaluated by estimating the collection efficiency at SEM detector by calculating the static electric and magnetic field distribution within the specimen chamber and then the trajectories for emitted SEs. We adopted a simplified 2D approach where we model the collection of SE as a function of emission position on the sample (representing a 1D cross-section of the surface).

15

Secondary Electrons are represented as being emitted from just outside the surface (3nm above), Lambertian distributed in angle (Slówko, 1999) and with a distribution of kinetic energy E_k detailed in the following. The physics of generation and transport of SE within the semiconducting perovskite film is accounted for by assuming a spectral distribution for the number *N* of emitted SE defined as (Cazaux, 2010; Henke et al., 1979):

$$dN/dE_k \sim f(E_k) = E_k/(E_k + \chi - E_g)^2 (E_k + \chi)^{5/2} \quad . \tag{3}$$

In Eq.3, E_k is the kinetic energy of emitted electrons in the vacuum, χ and E_g are respectively the electron affinity and the bandgap of the material. For the MAPbI$_3$ layer, $f(E_k)$ has been evaluated by choosing $\chi = 3.93eV$ as educated guess value for the electron affinity (Zhao et al., 2015) and $E_g = 1.6 \ eV$ for the amplitude of the bandgap (present work). The resulting spectral distribution is plotted in Fig.11, with a maximum in the SE emission probability located at $0.85eV$ a. Then the simulation focuses onto the process of collection of emitted SEs in the presence of surface photoinduced local potentials. In correspondence to each emission point at sample surface the SE total collection is evaluated by integrating different E_k contribution curves and using $f(E_k)$ as the relative weighting function. In particular, we used E_k values over the $0.1eV - 15$ eV range, considering that this portion of the spectrum contributes more than 90% of the overall SE emission. In this way, the SE contrast energy profiles modified by the collection efficiency result in emission point dependent SE collection yields at the detector in dependence on the emission points.
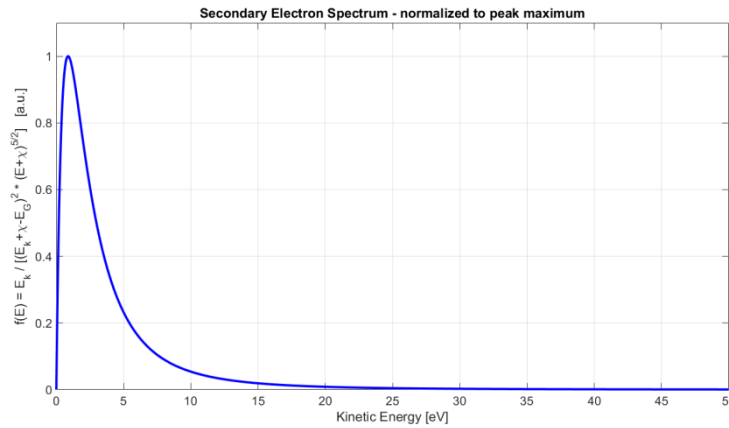

Fig.11 : SE emission function for MAPbI$_3$, calculated up to E$_k$=50eV, for $\chi = 3.93eV, E_g = 1.6eV$ as guess values, respectively for the electron affinity and the bandgap in MAPbI$_3$.
[NO COLOR PRINT]-[SMALL COLUMN SIZE]

Detector and electron column are defined as metal electrodes with assigned values of potentials, which are boundary conditions for the resolution of the Laplace equation in free space. Namely, the detector is modeled as an ~~simple~~ electrode (representing the acceleration grid) at $V = +300 \ V$, while the electron column is set at 0V. Also the sample bulk is grounded and represented as a rectangle 1cm-wide positioned at 5mm from the electron column. ~~On the contrary,~~ At the sample top surface a potential distribution ~~is inserted, modeled as~~ with a normal distribution of standard deviation σ = 50μm and peak amplitude V_{pk} ~~This~~ models the effects of the laser beam photoexcitation, under the hypothesis of Gaussian beam cross-sectional profile and above-bandgap linear absorption of incident photons. The surface photo-excited potential results from the unbalanced charge distribution between the sample surface and the bulk, the amplitude of which is Gaussian-distributed

in the plane of the sample -but for the projection factor $1/\cos{(\gamma)}$- resulting in an elliptical cross-section. Also the surface potential calculated along the points of the axes of the illuminated ellipse is a bell-shaped function which can be approximated by a normal function.

The spatialy modulated surface potential affects the trajectories of the SE in an emission point dependent way. The signal from the ET detector is substantially proportional to the number of SE entering the SEM column, spatially filtered by the effective collection angle. The effective collection angle, referred to the sample normal, is defined as the averaged maximum emission angle of the electrons that arrive on the detector; specifically, the average is performed over the significant energy interval of [0eV, 15eV] of the spectral distribution of SE and for a sample potential kept at 0V. In case of sample horizontally aligned at θ=0, an effective collection angle of $\sim 2 deg$ is estimated, by accounting for the angular and spectral SE emission.

4.   Discussion

Bright and dark contrast areas in SEM images as in Fig.10 correspond respectively to regions of higher or lower SE collection, resulting from the spectral distribution of emitted SEs as well as from their trajectories to the detector (Cazaux, 2012, 2010). A key to the interpretation of TR-SEM contrast patterns is provided by comparing measured differential $C_{i,j}^N$ profiles and numerically simulated profiles of SE collection yield, in the presence of a local surface potential distribution. Therefore, experimental $C_{i,j}^N$ cross sectional profiles have been extracted across the laser footprint in TR-SEM patterns and compared to simulated SE collection profiles.

It is evident that experimental cross-sectional profiles are deeply affected by the value of tilt angle θ. For instance, in Fig. 8 variations in θ transform the dark pattern measured in correspondence to the illuminated area at $\theta = 0$ into a dipolar contrast. In other words, if the negative contrast which is registered under conditions of z-axis symmetry at $\theta = 0$ indicates that a localized reduction in SE collection occurs as a consequence of above-bandgap photon absorption in MAPbI$_3$ film, *asymmetric* detection at $\theta \neq 0$ advises that this may not be due merely to a depressed value of SE emission in the illuminated spot.

For an insightful analysis of the experimental results, accordingly, two reference simulation geometries are chosen. The first case, z-axis *symmetric*, is described in Fig. 12 and refers to horizontal sample $(\theta = 0)$, with its surface normal directed along the column axis. All the SE emission points located at the sample surface are equidistant from the SEM column. This case removes any possible collection effects due to geometrical asymmetries, stressing the importance of local distribution of potentials at sample surface in affecting the SE contrast map. Fig. 12a shows the 2D section of the specimen chamber as it looks in the simulation environment. The relative positions of the sample, the column and the ET detector are in scale. The insets show the potential distribution in the chamber volume and the trajectories for emitted SEs, (1) in the cases of absence of illumination (the sample is grounded and $V_{pk} = 0$) and by admitting that a local voltage distribution is excited at the sample surface, with normal distribution centered with the column axis and peaked at $V_{pk} =+ 5V$, performing a lensing effect (2,3). Specifically, case 2 (3) shows the trajectories of SE emitted from a surface point aligned with the column axis and with kinetic energies slightly below (above) eV_{pk}. Case (3) In the latter case graphs refers to a test positive value , and

show the lensing effect which modifies the trajectories of emitted electrons. In the simplified case of SE emitted from the center of the sample, as in the insets of Fig. 12, only those at $E_k > eV_{pk}$ are collected (Cazaux, 2010). By accounting for SE emission points over all the illuminated area, less energetic electrons are generally less collected than higher energetic ones. When also considering the relative higher contribution of the less energetic SEs to the detected signal, as expressed by the spectral function $f(E_k)$, an overall dark SE contrast is generated. Simulated and experimental contrast profiles for this symmetric case ($\theta = \phi = 0$) are compared in Fig. 12b, referred to a post-illumination case ($\theta = 0$ in Fig.8). Measured and simulated dark profiles are in good agreement, suggesting that a contribution to dark differential contrast patterns over illuminate regions can be contributed by positive values of photoinduced local surface potentials. The insets show, on the right, the geometry of cross-sectioning of SE contrast patterns and, on the left, the comparison among simulated contrast profiles at different values of $V_{pk} > 0$, showing that electrons emitted closer to the optical axis experience larger collection efficiencies, that may turn in positive contrast. Left-right asymmetries in the profiles that may arise from the asymmetrical position of the detector within the electron column are negligible in this case.
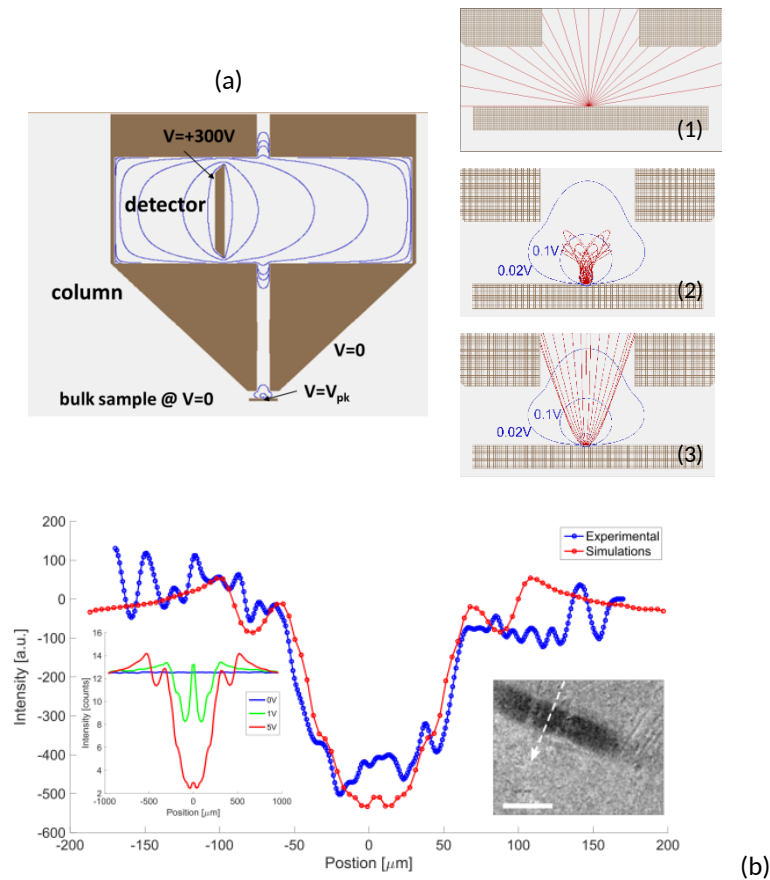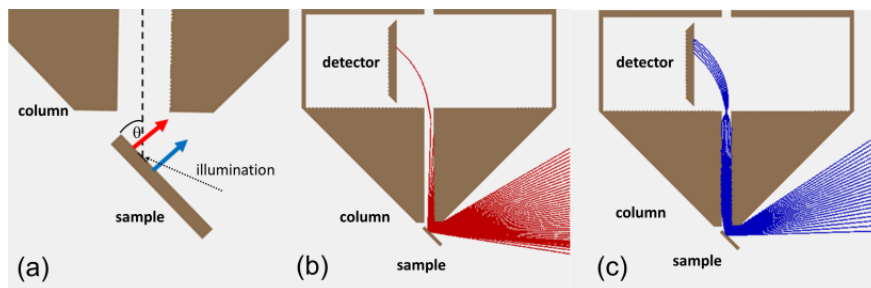
Fig. 12: detection of TR-SEM patterns in case of horizontal sample ($\underline{\theta = 0}$). (a) Schematic representation of 2D simulation environment, showing the relative positions of the sample, the column and the ET detector. The insets show the potential distribution in the chamber volume and trajectories for emitted SEs <u>from a surface point on the column axis,</u> in the absence of illumination (1) and by admitting that a local voltage distribution is excited (2,3), showing its lensing effect on SE emitted from the center of the sample. For V_{pk}>0, only SE at E_k>V_{pk} are collected. (b): Comparison of experimental TR-SEM contrast pattern and simulated contrast profile across the optically excited region, referring to a post-illumination case and by admitting V_{pk}=+ 5V. The insets show the comparison among simulated contrast profiles at different values of photoinduced potentials, and the geometry of cross-sectioning of measured SE contrast pattern. <u>(200 μm scale mark)</u>
[NO COLOR PRINT]-[1.5 COLUMN SIZE]

The second simulated geometry addresses the role of local potential in case of sample tilted at $\theta = 45°$ and is shown in Fig. 13. The degeneracy in distance between SE emission points and the entrance of the *in-column* detection system is removed and, by accounting for relative position of SE emission points with respect to the distribution of local photoexcited space charge, additional information is conveyed. Specifically, Fig. 13a is a sketch of tilted sample, where red (blue) arrows indicate the emission of SE from points on the surface respectively located closer (farther) to the entrance of the column than the center <u>of the</u> illuminated spot. The effect of a positive potential distribution located at the illuminated spot is to decrease electron collection from the points <u>located c</u>loser to the column and to improve collection from ~~farther~~ points located farther from it, as shown by the SE trajectories plotted in Fig. 13b and 13c respectively. The overall effect on the population of emitted SEs is equivalent to that shown in Fig. 13d, where an experimental cross section measured in dark 60s after turning laser off (also shown in Fig.10a) is compared with simulated profile obtained for V_{pk}=+ 5V. Also in tilted geometry, the matching of the experimental and simulated trends for SE collection implies that experimental results are consistent with the existence of a localized region of positive voltage at sample surface. This suggests that, as soon as the laser beam is turned off, over time constants of several seconds a net positive voltage distribution builds-up at the surface of MAPbI$_3$.
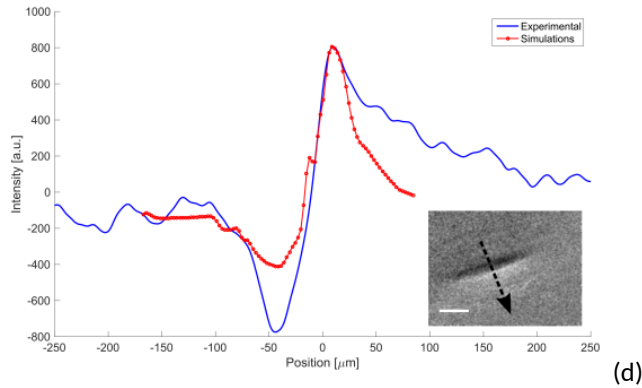
(d)

Fig. 13: detection of TR-SEM patterns in case of tilted sample ($\theta = 45°$). (a) Schematic representation of 2D simulation environment, showing the relative positions of the sample and the column and the position of the illuminated spot. The arrows indicate respectively SE emission points closer to the entrance to the column than the illuminated region (red arrow), or farther from it (blue arrow), respectively. (b),(c): trajectories of collected electrons, emitted respectively from points located closer to the entrance of the column (red), or farther from it (blue) respectively , by admitting that a local surface potential of peak value $V_{pk} = + 5V$ exists at the illuminated site. (d): Comparison of experimental TR-SEM contrast pattern and simulated contrast profile across the optically excited region, referring to a post-illumination case and by admitting $V_{pk} = + 5V$. In the inset, the geometry of cross-sectioning of measured SE contrast pattern. (200 µm scale mark)

[NO COLOR PRINT]-[1.5 COLUMN SIZE]

SE collection profiles have also been simulated by admitting that a negatively polarized area is induced on the sample. Fig.14 compares the test cases of $V_{pk} = \pm 5V$, calculated in asymmetric geometry. Evidently in <u>the case of a negative potential</u> the contrast pattern is coarsely reversed with respect to the <u>case of a positive potential, similar to </u>experimentally measured one. On the other hand, the profiles show evident shape differences, which reduce the superposition of the first profile with the ~~sign~~ <u>horizontal-</u>reversal of the second (indicated by the <u>gray </u>dotted line). This effect is <u>attributed</u> to <u>the ~~enhanced~~</u> breaking of symmetry due to the lateral position of the detector.
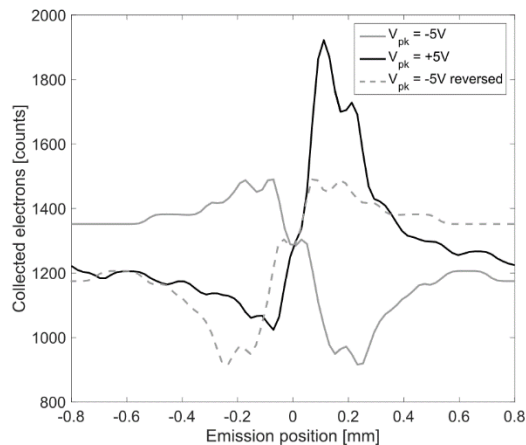

Fig. 14: Comparison of simulated profiles for SE collection at the detector, contributed by electrons at $E_k = 5eV$, in the presence of a localized and Gaussian-shaped region of positive (blackline) and negative (gray line) surface potential, in tilted geometry. Measured TR-SEM profiles are in accordance with the generation of a positive voltage in the illuminated region.

20

For sake of comparison, a <u>horizontally</u> reversed replica of the green profile at negative surface potential is also shown (dotted <u>gray</u> line), to be compared to the red profile. Differences can be ascribed to symmetry breaking due to the combination of tilted geometry an of the lateral position of the detector.
[NO COLOR PRINT]-[SMALL COLUMN SIZE]

Even if a detailed explanation of the photo-physics at the origin of the space charge distribution detected by TR-SEM is beyond the scope of the present work, TR-SEM findings illustrated here support some of the interpretative models proposed in the literature and provide a strong theoretical framework to investigate the photoinduced dynamics at surface of perovskite and other semiconductor materials, on long and, in perspective, also on short timescales. Namely, TR-SEM patterns are consistent with the hypothesis that a positive space charge distribution develops at the surface of perovskite thin films after illumination at photon energies exceeding the bandgap, which evolves over time scales of the order of several minutes. Equilibrium conditions are eventually recovered over a few hours. Since free carriers injected in perovskite films recombine in sub-second timescales (Sarritzu et al., 2017; Xiao et al., 2014b), slowly evolving contrast is an indication that the space charge field at surface is of ionic origin.

Specifically, in the present case strongly absorbed blue light induces a gradient of illumination, which may issue a segregation of positive charge at the film surface and a migration of negative charge towards the back. The building-up of a positive space charge configuration at the surface of $MAPbI_3$ films may be consistent with photoinduced migration of negative I^- ions away from the surface and towards the PEDOT:PSS layer under the effect of concentration gradients and charge effects (Deng et al., 2015b; Xiao et al., 2014b), the mobility <u>of iodide</u> being greatly enhanced under illumination (Xing et al., 2016). Ion mobility is one major cause in the degradation of performances of perovskite solar cells (Barker et al., 2017; Xing et al., 2016). However, the present result show that charge redistribution may also occur in the absence of a complete device, and when just the free surface (*neat*) $MAPbI_3$ film is considered as in the present case. The migration of I^- away from blue-light illuminated surface in neat perovskite films, without electrical contacts, has also been proven by chemical mapping using Time-of-Flight Second-Ion-Mass-Spectroscopy (ToF-SIMS) (deQuilettes et al., 2016).

Upon light removal <u>the</u> temporal dynamics registered in TR-SEM express a slow recovery of the system to its pristine state , which takes up to several hours <u>to recover. Again, this is</u> compatible with what is assessed by complementary research in the literature on photoinduced chemical and structural transformation of perovskite films (deQuilettes et al., 2016; Gottesman et al., 2015). Regarding the amplitude of the photoinduced electrostatic voltage, <u>an electrical biasing in the range of 1V builds up across the 300nm-thick perovskite film, in a model where the illuminated $MAPbI_3$ film acts as a capacitor and by admitting that a net charge density of about $10^{17} - 10^{18} cm^{-3}$ is optically excited over a depth of $\alpha^{-1} = 100nm$ (which is fully compatible with reported data in the literature related to the concentration of defects (Wang et al., 2014; Xiao et al., 2015)). In case of passivation of the top surface of the film, as it is obtained by depositing the ETL layer in a complete solar cell structure, quite different local charge transport conditions and surface values of photovoltage may arise.</u>
The building up of a dark and rather uniform contrast under CW illumination, as shown in Fig. 10, deserves a different discussion. It can <u>be</u> admitted that above-bandgap blue laser light is absorbed within the $MAPbI_3$ thickness (Stranks et al., 2014) and excites a free carrier population in the range of $10^{16} \div 10^{17} cm^{-3}$ within 100 nm from the surface, as can be calculated by solving drift-diffusion rate equations. Semiconducting $MAPbI_3$ thin films grown by the two-step interdiffusion method on PEDOT:PSS are generally of p-type (Xiao et al., 2014b). In turn, p-type semiconductors are reported to show a

brighter SEM signal than n-type ones, also due to a favorable surface band bending and local work function reduction induced by the presence of charged surface defect states (Cazaux, 2012; El-Gomati et al., 2004). In the illuminated area, as a consequence of the density of photoexcited free carriers, screening of the surface charges and band flattening occurs (Kronik and Shapira, 1999), that locally increases the work function value and decreases the SE collection yield. Such a phenomenon is similar to a local dynamic photo-doping of the surface of the perovskite material, which turns more n-type, so that collection effects similar to those happening in *pn* junction geometries become temporally evident (De Bastiani et al., 2016; Deng et al., 2015b). The result is a dark differential TR-SEM contrast, which instantaneously follows the switching ON and OFF of the illumination under present experimental conditions.

5. CONCLUSIONS

Time-Resolved laser-assisted SEM (TR-SEM) provides dynamical mapping of *in-situ* excited photo-physical and photo-chemical phenomena at surfaces, with nanoscale resolution and large field of view. In the present work optically excited SE contrast patterns are recorded at subsequent temporal intervals and over timescales compatible with real-time SEM imaging. Differential processing of detected SE images allows to disentangle the optically excited contribution to SE contrast from the morphological background. The information on the photoexcited surface dynamics provided by TR-SEM crucially depends on the geometry and boundary condition of the detection process, which are modeled in the framework of static electric and magnetic field calculation and ray-tracing of SE electron trajectories.

In its present proof-of-concept implementation, TR-SEM provides qualitative dynamical imaging of the long term evolution in the charge fields, optically excited and segregated at film surface. A more quantitative approach can be developed, by introducing a finer numerical modelling of the actual SEM specimen chamber geometry and of SE collection process. For a thorough quantitative evaluation, through the fitting with simulated patterns, also the modifications in the SE emission curve introduced by intense optical irradiation and related effects in the material should be taken into account (Cazaux, 2011), to correlate the gray levels corresponding to differential contrast values C_{ij}^N with the surface voltage, through the fitting with simulated patterns.

Real time TR-SEM is applied to visualize long-term dynamics of photoinduced potentials at the free surface of $MAPbI_3$ perovskite thin films deposited onto conductive PEDOT:PSS and illuminated by above-bandgap blue laser light at λ=405nm. Permanent damaging of the material is avoided by operating the TR-SEM at 5keV of PE energy and 1-10pA of primary current, even under intense optical excitation up to $50W/cm^2$. As the $MAPbI_3$ film is illuminated by focused light, SE contrast patterns build up on the temporal scale of seconds and evolve in the dark after light removal, with time constants of several minutes. A nearly complete recovery of pristine conditions is achieved within days. By performing measurements at different orientations of the sample with respect to the SEM column axis, and by comparing measured contrast profiles with results from a 2D numerical model, TR-SEM patterns can be attributed to the buildup and evolution of local space charge fields. Specifically, in the light of the studies on photovoltaic perovskites and related photoinduced charge transport, TR-SEM results supports the hypothesis of slow motion and reconfiguration of the ionic species in the $MAPbI_3$ polycrystalline

samples under illumination, leading to optical excitation of a local positive potential at surface and to its recovery over timescales of hours.

The overall depression in SE emission which is observed under illumination is also contributed by a phenomenon of optical poling of the MAPbI$_3$, which near its surface ~~from *p*-type~~ turns into *n*-type from *p*-type and increases the barrier to SE emission.

The reversible dynamics of photoinduced phenomena in MAPbI$_3$ even at high optical intensities, as displayed by TR-SEM, is appealing in view of applications of the material in concentrated photovoltaics and as an active material for light generation. <u>A more</u> detailed explanation regarding the physical and chemical mechanisms at the basis of TR-SEM induced dynamical contrast in hybrid perovskites will be presented elsewhere.

In perspective, thanks to its surface mapping capability, TR-SEM can support investigations on the photo-physics and working principles of photoelectrical and photovoltaic material systems and devices, in thin films and low-dimensional structures. <u>Besides being effective in the dynamical probing of spatially-resolved photoelectric response of materials, as a tool TR-SEM can support investigation on their fatigue, damaging and long term degradation.</u>

REFERENCES

Ali Deeb, M., Ledig, J., Wei, J., Wang, X., Wehmann, H.H., Waag, A., 2017. Photo-assisted Kelvin probe force microscopy investigation of three dimensional GaN structures with various crystal facets, doping types, and wavelengths of illumination. J. Appl. Phys. 122, 0–7. https://doi.org/10.1063/1.5000137

Barker, A.J., Sadhanala, A., Deschler, F., Gandini, M., Senanayak, S.P., Pearce, P.M., Mosconi, E., Pearson, A.J., Wu, Y., Srimath Kandada, A.R., Leijtens, T., De Angelis, F., Dutton, S.E., Petrozza, A., Friend, R.H., 2017. Defect-Assisted Photoinduced Halide Segregation in Mixed-Halide Perovskite Thin Films. ACS Energy Lett. 2, 1416–1424. https://doi.org/10.1021/acsenergylett.7b00282

Cazaux, J., 2012. From the physics of secondary electron emission to image contrasts in scanning electron microscopy. J. Electron Microsc. (Tokyo). 61, 261–284. https://doi.org/10.1093/jmicro/dfs048

Cazaux, J., 2011. Calculated effects of work function changes on the dispersion of secondary electron emission data: Application for Al and Si and related elements. J. Appl. Phys. 110. https://doi.org/10.1063/1.3608046

Cazaux, J., 2010. Material contrast in SEM: Fermi energy and work function effects. Ultramicroscopy. https://doi.org/10.1016/j.ultramic.2009.12.002

Cazaux, J., 2008. On some contrast reversals in SEM: Application to metal/insulator systems. Ultramicroscopy. https://doi.org/10.1016/j.ultramic.2008.06.005

Cazaux, J., 2004. Charging in scanning electron microscopy "from inside and outside". Scanning 26, 181–203. https://doi.org/10.1002/sca.4950260406

Chee, A.K.W., Broom, R.F., Humphreys, C.J., Bosch, E.G.T., 2011. A quantitative model for doping contrast in the scanning

electron microscope using calculated potential distributions and Monte Carlo simulations. J. Appl. Phys. 109, 1–9. https://doi.org/10.1063/1.3524186

Chee, K.W.A., Rodenburg, C., Humphreys, C.J., 2008. High resolution dopant profiling in the SEM, image widths and surface band-bending. J. Phys. Conf. Ser. 126. https://doi.org/10.1088/1742-6596/126/1/012033

Chiarello, G.L., Bernareggi, M., Pedroni, M., Magni, M., Pietralunga, S.M., Tagliaferri, A., Vassallo, E., Selli, E., 2017. Enhanced photopromoted electron transfer over a bilayer WO_3 n-n heterojunction prepared by RF diode sputtering. J. Mater. Chem. A 5, 12977–12989. https://doi.org/10.1039/c7ta03887a

Cho, J., Hwang, T.Y., Zewail, A.H., 2014. Visualization of carrier dynamics in p(n)-type GaAs by scanning ultrafast electron microscopy. Proc. Natl. Acad. Sci. 111, 2094–2099. https://doi.org/10.1073/pnas.1400138111

De Bastiani, M., Dell'Erba, G., Gandini, M., D'Innocenzo, V., Neutzner, S., Kandada, A.R.S., Grancini, G., Binda, M., Prato, M., Ball, J.M., Caironi, M., Petrozza, A., 2016. Ion migration and the role of preconditioning cycles in the stabilization of the J-V characteristics of inverted hybrid perovskite solar cells. Adv. Energy Mater. 6, 1–9. https://doi.org/10.1002/aenm.201501453

Deng, Y., Xiao, Z., Huang, J., 2015a. Light-induced self-poling effect on organometal trihalide perovskite solar cells for increased device efficiency and stability. Adv. Energy Mater. 5, 1–6. https://doi.org/10.1002/aenm.201500721

deQuilettes, D.W., Zhang, W., Burlakov, V.M., Graham, D.J., Leijtens, T., Osherov, A., Bulović, V., Snaith, H.J., Ginger, D.S., Stranks, S.D., 2016. Photo-induced halide redistribution in organic–inorganic perovskite films. Nat. Commun. 7, 11683. https://doi.org/10.1038/ncomms11683

Drouin, D., Couture, A.R., Joly, D., Tastet, X., Aimez, V., Gauvin, R., 2007. CASINO V2.42 - A fast and easy-to-use modeling tool for scanning electron microscopy and microanalysis users. Scanning 29, 92–101. https://doi.org/10.1002/sca.20000

Egerton, R.F., Li, P., Malac, M., 2004. Radiation damage in the TEM and SEM. Micron 35, 399–409. https://doi.org/10.1016/j.micron.2004.02.003

El-Gomati, M., Zaggout, F., Jayacody, H., Tear, S., Wilson, K., 2005. Why is it possible to detect doped regions of semiconductors in low voltage SEM: A review and update. Surf. Interface Anal. 37, 901–911. https://doi.org/10.1002/sia.2108

El-Gomati, M.M., Wells, T.C.R., 2001. Very-low-energy electron microscopy of doped semiconductors. Appl. Phys. Lett. 79, 2931–2933. https://doi.org/10.1063/1.1415045

El-Gomati, M.M., Wells, T.C.R., Müllerová, I., Frank, L., Jayakody, H., 2004. Why is it that differently doped regions in semiconductors are visible in low voltage SEM? IEEE Trans. Electron Devices 51, 288–292. https://doi.org/10.1109/TED.2003.821884

Elliott, S.L., Broom, R.F., Humphreys, C.J., 2002. Dopant profiling with the scanning electron microscope - A study of Si. J. Appl. Phys. 91, 9116–9122. https://doi.org/10.1063/1.1476968

Flesner, L.D., 1992. Apparatus and method for non-contact surface voltage probing by scanning photoelectron emission. 5150043.

Flesner, L.D., 1990. Scanning Electron Microscopy by photovoltage contrast imaging. 4902967.

Gomez, A., Sanchez, S., Campoy-Quiles, M., Abate, A., 2018. Topological distribution of reversible and non-reversible degradation in perovskite solar cells. Nano Energy 45, 94–100. https://doi.org/10.1016/j.nanoen.2017.12.040

Gottesman, R., Gouda, L., Kalanoor, B.S., Haltzi, E., Tirosh, S., Rosh-Hodesh, E., Tischler, Y., Zaban, A., Quarti, C., Mosconi, E., De Angelis, F., 2015. Photoinduced reversible structural transformations in free-standing $CH_3NH_3PbI_3$ perovskite films. J. Phys. Chem. Lett. 6, 2332–2338. https://doi.org/10.1021/acs.jpclett.5b00994

Henke, B.L., Liesegang, J., Smith, S.D., 1979. Soft-x-ray-induced secondary-electron emission from semiconductors and insulators: Models and measurements. Phys. Rev. B 19, 3004–3021. https://doi.org/10.1103/PhysRevB.19.3004

Hoke, E.T., Slotcavage, D.J., Dohner, E.R., Bowring, A.R., Karunadasa, H.I., McGehee, M.D., 2015. Reversible photo-induced trap formation in mixed-halide hybrid perovskites for photovoltaics. Chem. Sci. 6, 613–617. https://doi.org/10.1039/C4SC03141E

Jana, D., Porwal, S., Sharma, T.K., Kumar, S., Oak, S.M., 2014. Pump-probe surface photovoltage spectroscopy measurements on semiconductor epitaxial layers Pump-probe surface photovoltage spectroscopy measurements on semiconductor epitaxial layers 043909, 0–9. https://doi.org/10.1063/1.4871990

Kazemian, P., Mentink, S.A.M., Rodenburg, C., Humphreys, C.J., 2006. High resolution quantitative two-dimensional dopant mapping using energy-filtered secondary electron imaging. J. Appl. Phys. 100. https://doi.org/10.1063/1.2335980

Konvalina, I., Müllerová, I., 2006. The trajectories of secondary electrons in the scanning electron microscope. Scanning 28, 245–56. https://doi.org/10.1002/sca.4950280501

Kronik, L., Shapira, Y., 2001. Surface photovoltage spectroscopy of semiconductor structures: At the crossroads of physics, chemistry and electrical engineering. Surf. Interface Anal. 31, 954–965. https://doi.org/10.1002/sia.1132

Kronik, L., Shapira, Y., 1999. Surface photovoltage phenomena: Theory, experiment, and applications. Surf. Sci. Rep. 37, 1–206. https://doi.org/10.1016/S0167-5729(99)00002-3

Lanzani, G., 2012. The Photophysics behind Photovoltaics and Photonics. Wiley-VCH.

Leijtens, T., Hoke, E.T., Grancini, G., Slotcavage, D.J., Eperon, G.E., Ball, J.M., De Bastiani, M., Bowring, A.R., Martino, N., Wojciechowski, K., McGehee, M.D., Snaith, H.J., Petrozza, A., 2015. Mapping electric field-induced switchable poling and structural degradation in hybrid lead halide perovskite thin films. Adv. Energy Mater. 5, 1–11. https://doi.org/10.1002/aenm.201500962

Liao, B., Najafi, E., 2017. Scanning ultrafast electron microscopy: A novel technique to probe photocarrier dynamics with high spatial and temporal resolutions. Mater. Today Phys. https://doi.org/10.1016/j.mtphys.2017.07.003

Manura, D., Dahl, D., 2008. SIMION 8.0 User Manual.

May, P., Halbout, J.M., Chiu, G., 1987. Picosecond photoelectron scanning electron microscope for noncontact testing of integrated circuits. Appl. Phys. Lett. 51, 145–147. https://doi.org/10.1063/1.98596

Mohammed, O.F., Yang, D.S., Pal, S.K., Zewail, A.H., 2011. 4D scanning ultrafast electron microscopy: Visualization of materials surface dynamics. J. Am. Chem. Soc. 133, 7708–7711. https://doi.org/10.1021/ja2031322

Müllerová, I., Konvalina, I., 2009. Collection of secondary electrons in scanning electron microscopes. J. Microsc. 236, 203–

210. https://doi.org/10.1111/j.1365-2818.2009.03189.x

NREL's "Best Research-Cell Efficiencies" Chart [WWW Document], 2018. URL https://www.nrel.gov/pv/assets/pdfs/pv-efficiencies-07-17-2018.pdf

Sarritzu, V., Sestu, N., Marongiu, D., Chang, X., Masi, S., Rizzo, A., Colella, S., Quochi, F., Saba, M., Mura, A., Bongiovanni, G., 2017. Optical determination of Shockley-Read-Hall and interface recombination currents in hybrid perovskites. Sci. Rep. 7. https://doi.org/10.1038/srep44629

Sealy, C.P., Castell, M.R., Wilshaw, P.R., 2000. Mechanism for secondary electron dopant contrast in the SEM. J. Electron Microsc. (Tokyo). 49, 311–321. https://doi.org/10.1093/oxfordjournals.jmicro.a023811

Seiler, H., 1983. Secondary electron emission in the scanning electron microscope. J. Appl. Phys. 54, R1–R18. https://doi.org/10.1063/1.332840

Slówko, W., 1999. Directional detection of secondary electrons for electron beam profilography. Vacuum 52, 441–449. https://doi.org/10.1016/S0042-207X(98)00329-7

Snaith, H.J., 2013. Perovskites: The emergence of a new era for low-cost, high-efficiency solar cells. J. Phys. Chem. Lett. 4, 3623–3630. https://doi.org/10.1021/jz4020162

Srimath Kandada, A.R., D'Innocenzo, V., Lanzani, G., Petrozza, A., 2016. Photophysics of Hybrid Perovskites, in: Unconventional Thin Film Photovoltaics. pp. 107–140. https://doi.org/10.1039/9781782624066-00107

Stranks, S.D., Stranks, S.D., Eperon, G.E., Grancini, G., Menelaou, C., Alcocer, M.J.P., Leijtens, T., Herz, L.M., Petrozza, A., Snaith, H.J., 2014. Electron-Hole Diffusion Lengths Exceeding. Science 342, 341–344. https://doi.org/10.1126/science.1243982

Tanaka, S.I., 2012. Utility and constraint on the use of pump-probe photoelectron spectroscopy for detecting time-resolved surface photovoltage. J. Electron Spectros. Relat. Phenomena 185, 152–158. https://doi.org/10.1016/j.elspec.2012.06.003

Tsurumi, D., Hamada, K., 2013. Sensitive site-specific dopant mapping in scanning electron microscopy on specimens prepared by low energy Ar+ ion milling. Appl. Phys. Express 6, 4–7. https://doi.org/10.7567/APEX.6.126201

Van Reenen, S., Kemerink, M., Snaith, H.J., 2015. Modeling Anomalous Hysteresis in Perovskite Solar Cells. J. Phys. Chem. Lett. 6, 3808–3814. https://doi.org/10.1021/acs.jpclett.5b01645

Volotsenko, I., Molotskii, M., Barkay, Z., Marczewski, J., Grabiec, P., Jaroszewicz, B., Meshulam, G., Grunbaum, E., Rosenwaks, Y., 2010. Secondary electron doping contrast: Theory based on scanning electron microscope and Kelvin probe force microscopy measurements. J. Appl. Phys. 107. https://doi.org/10.1063/1.3276090

Wang, Q., Shao, Y., Xie, H., Lyu, L., Liu, X., Gao, Y., Huang, J., 2014. Qualifying composition dependent p and n self-doping in CH3NH3PbI3. Appl. Phys. Lett. 105, 3–9. https://doi.org/10.1063/1.4899051

Wu, Y., Xie, F., Chen, H., Yang, X., Su, H., Cai, M., Zhou, Z., Noda, T., Han, L., 2017. Thermally Stable MAPbI3Perovskite Solar Cells with Efficiency of 19.19% and Area over 1 cm2achieved by Additive Engineering. Adv. Mater. 29, 1–8. https://doi.org/10.1002/adma.201701073

Wuerfel, P., 2009. Physics of Solar Cells, 2nd Ed. Wiley-VCH.

Xiao, Z., Bi, C., Shao, Y., Dong, Q., Wang, Q., Yuan, Y., Wang, C., Gao, Y., Huang, J., 2014a. Efficient, high yield perovskite

photovoltaic devices grown by interdiffusion of solution-processed precursor stacking layers. Energy Environ. Sci. 7, 2619–2623. https://doi.org/10.1039/c4ee01138d

Xiao, Z., Dong, Q., Bi, C., Shao, Y., Yuan, Y., Huang, J., 2014c. Solvent Annealing of Perovskite-Induced Crystal Growth for Photovoltaic-Device Efficiency Enhancement. Adv. Mater. 26, 6503–6509. https://doi.org/10.1002/adma.201401685

Xiao, Z., Yuan, Y., Shao, Y., Wang, Q., Dong, Q., Bi, C., Sharma, P., Gruverman, A., Huang, J., 2015. Giant switchable photovoltaic effect in organometal trihalide perovskite devices. Nat. Mater. 14, 193–197. https://doi.org/10.1038/nmat4150

Xing, J., Wang, Q., Dong, Q., Yuan, Y., Fang, Y., Huang, J., 2016. Ultrafast ion migration in hybrid perovskite polycrystalline thin films under light and suppression in single crystals. Phys. Chem. Chem. Phys. 18, 30484–30490. https://doi.org/10.1039/c6cp06496e

Xu, L., Weber, K., Phang, S.P., Fell, A., Brink, F., Yan, D., Yang, X., Franklin, E., Chen, H., 2013. Secondary electron microscopy dopant contrast image (SEMDCI) for laser doping. IEEE J. Photovoltaics 3, 762–768. https://doi.org/10.1109/JPHOTOV.2013.2241820

Yamada, Y., Nakamura, T., Endo, M., Wakamiya, A., Kanemitsu, Y., 2014. Photocarrier recombination dynamics in perovskite CH3NH3PbI3for solar cell applications. J. Am. Chem. Soc. 136, 11610–11613. https://doi.org/10.1021/ja506624n

Yuan, H., Debroye, E., Janssen, K., Naiki, H., Steuwe, C., Lu, G., Moris, M., Orgiu, E., Uji-I, H., De Schryver, F., Samorì, P., Hofkens, J., Roeffaers, M., 2016. Degradation of Methylammonium Lead Iodide Perovskite Structures through Light and Electron Beam Driven Ion Migration. J. Phys. Chem. Lett. 7, 561–566. https://doi.org/10.1021/acs.jpclett.5b02828

Zani, M., Sala, V., Irde, G., Pietralunga, S.M., Manzoni, C., Cerullo, G., Lanzani, G., Tagliaferri, A., 2018. Charge dynamics in aluminum oxide thin film studied by ultrafast scanning electron microscopy. Ultramicroscopy 187. https://doi.org/10.1016/j.ultramic.2018.01.010

Zhao, Y., Liang, C., Zhang, H., Li, D., Tian, D., Li, G., Jing, X., Zhang, W., Xiao, W., Liu, Q., Zhang, F., He, Z., 2015. Anomalously large interface charge in polarity-switchable photovoltaic devices: An indication of mobile ions in organic-inorganic halide perovskites. Energy Environ. Sci. 8, 1256–1260. https://doi.org/10.1039/c4ee04064c

Light-induced modifications at grain boundaries in SEM imaging

SEM images were taken at a magnification M=50k X, to highlight the grain morphology at film surface.

Images were taken before and after laser irradiation, as described in Figure 4 and here reported in Figure S.I.1. The differential image – digitally realigned to compensate for mechanical drift of the stage – suggests that under present experimental conditions negligible morphological damage is induced. Contrast variations in the differential image in correspondence to grain boundaries might be contributed by light-induced long-lasting local space-charge domains, in agreement with what recently investigated e.g. by Gomez and co-workers by Photoconductive AFM and PL microscopy (Gomez et al., 2018).
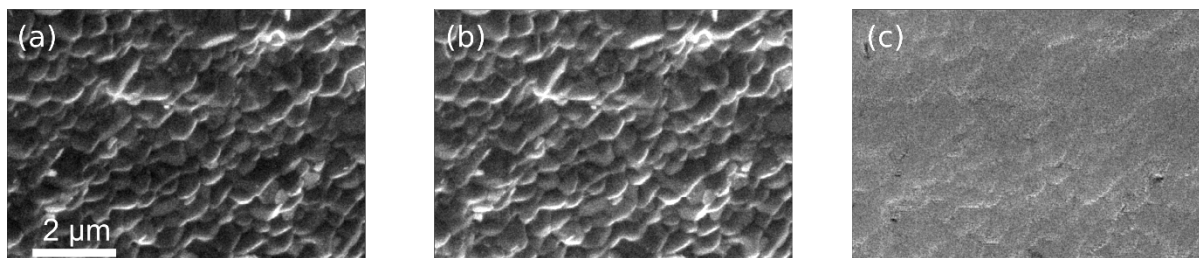

Figure S.I.1.: SEM high magnification images M=50k of the pristine area of MAPbI3 sample (a) and after being irradiated at $I \sim 50 W cm^{-2}$ for 480 seconds (b), showing no evidence of optically induced morphological damaging. (c) Differential processing of images (b)-(a) to enhance possible light-induced modifications at the grain level. Images have been realigned, to partially take into account the thermally induced mechanical drift of the stage. Realignment of the images was performed by maximizing the 2D cross-correlation between images (a) and (b).

Effects of C contamination on SEM contrast and light-induced TR-SEM

In order to avoid the effects induced by e-beam-assisted hydrocarbon contamination on TR-SEM contrast results, a damaging threshold for the electron dose – defined as the number of electrons deposited over a specific area and measured in electrons/cm^2- was experimentally defined. At fixed values of primary electron (PE) current, the electron dose increases with magnification. Therefore, in order to visualize contamination effects induced by the electron beam on MAPbI$_3$, the following process was established. At a defined value for the PE current a first SEM image was acquired at magnification M= 1500X; then, a second image was acquired on the same spot at lower magnification M = 300X. In this way, the frame of the former image at higher magnification (also corresponding to higher electron dose) is fully contained within the field of view of the latter and a darker frame is imaged in case of contamination.

The process is described in Figure SI.2. Figure SI.2(a) shows the reference scheme of the image frame at M=300X, which contains the frame at M=1500X. Figures SI.2(b-d) are images taken at M=300X and that include the frames at M=1500X and scanned at electron doses respectively of $5 \times 10^{13} el/cm^2$, $2 \times 10^{14} el/cm^2$ and $5 \times 10^{14} el/cm^2$. Contamination marks can be perceived starting from an electron dose of $\sim 10^{14} el/cm^2$, which can be taken as the threshold value.
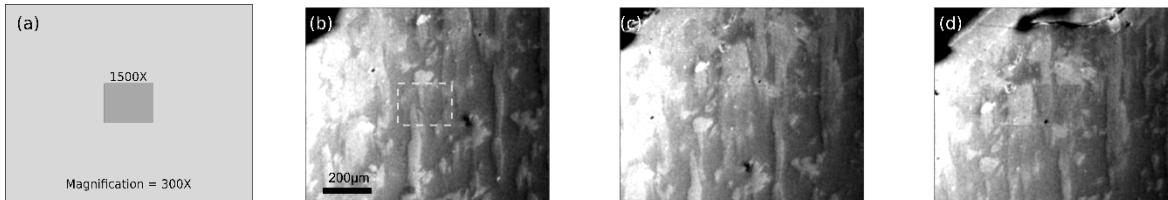

Figure SI.2. Characterisation of the electron beam effect on MAPbI$_3$. (a) Measurement scheme: an image at M = 1500X is acquired; then the effect is monitored on a frame at M = 300X. (b-d): Images represent overviews (300X) with inner frames (1500X) scanned at electron doses of: $5 \times 10^{13} el/cm^2$, $2 \times 10^{14} el/cm^2$ and $5 \times 10^{14} el/cm^2$. Dashed rectangle in (b) is a guide for the eyes. Images contrast has been enhanced to highlight electron beam marks.

References

Gomez, A., Sanchez, S., Campoy-Quiles, M., Abate, A., 2018. Topological distribution of reversible and non-reversible degradation in perovskite solar cells. Nano Energy 45, 94–100. https://doi.org/10.1016/j.nanoen.2017.12.040